HHS Public Access

Author manuscript

J Magn Reson Imaging. Author manuscript; available in PMC 2019 November 01.

Published in final edited form as:

J Magn Reson Imaging. 2019 October ; 50(4): 1207–1218. doi:10.1002/jmri.26664.

3D-$T_{1\rho}$ Prepared Zero Echo Time-Based PETRA Sequence for In Vivo Biexponential Relaxation Mapping of Semisolid Short-T_2 Tissues at 3 T

Azadeh Sharafi, PhD[*], **Rahman Baboli, MS**, **Gregory Chang, MD**, **Ravinder R. Regatte, PhD**

Bernard and Irene Schwartz Center for Biomedical Imaging, Department of Radiology, New York University School of Medicine, New York New York, USA

Abstract

Background: In addition to the articular cartilage, osteoarthritis (OA) affects several other tissues such as tendons, ligaments, and subchondral bone. $T_{1\rho}$ relaxation study of these short T_2 tissues may provide a more comprehensive evaluation of OA.

Purpose: To develop a 3D spin-lattice relaxation in the rotating frame ($T_{1\rho}$) prepared zero echo time (ZTE)-based pointwise encoding time reduction with radial acquisition (3D-$T_{1\rho}$-PETRA) sequence for relaxation mapping of semisolid short-T_2 tissues on a clinical 3 T scanner.

Study Type: Prospective.

Population: Phantom, two bovine whole knee joint and Achilles tendon specimens, 10 healthy volunteers with no known inflammation, trauma or pain in the knee or ankle.

Field Strength/Sequence: A customized PETRA sequence to acquire fat-suppressed 3D $T_{1\rho}$-weighted images tissues with semisolid short T_2/T_2^* relaxation times in the knee and ankle joints at 3 T.

Assessment: Mono- and biexponential $T_{1\rho}$ relaxation components were assessed in the patellar tendon (PT), anterior cruciate ligament (ACL), posterior cruciate ligament (PCL), and Achilles tendon (AT).

Statistical Tests: Kruskal–Wallis with post-hoc Dunn's test for multiple pairwise comparisons.

Results: Phantom and ex vivo studies showed the feasibility of $T_{1\rho}$ relaxation mapping using the proposed 3D-$T_{1\rho}$-PETRA sequence. The in vivo study demonstrated an averaged mono-$T_{1\rho}$ relaxation of (median [IQR]) 15.9 [14.5] msec, 23.6 [9.4] msec, 17.4 [7.4] msec, and 5.8 [10.2] msec in the PT, ACL, PCL, and AT, respectively. The bicomponent analysis showed the short and long components (with their relative fractions) of 0.65 [1.0] msec (46.9 [15.3]%) and 37.3 [18.4] msec (53.1 [15.3]%) for PT, 1.7 [2.1] msec (42.5 [12.5]%) and 43.7 [17.8] msec (57.5 [12.5]%) for ACL, and 1.2 [1.9] msec (42.6 [14.0]%) and 27.7 [14.7] msec (57.3 [14.0]%) for PCL and 0.4 [0.02] msec (58.8 [13.3]%/) and 31.3 [10.8] msec (41.2 [13.3]%) for AT. Statistically significant

[*]Address reprint requests to: A.S., Bernard and Irene Schwartz Center for Biomedical Imaging, Department of Radiology, New York University School of Medicine, 660 1 Ave., 4 Fl., New York, NY, 10016. azadeh.sharafi@nyulangone.org.

Additional supporting information may be found in the online version of this article.

($P \leq 0.05$) differences were observed in the mono- and biexponential relaxation between several regions.

Data Conclusion: The 3D-$T_{1\rho}$-PETRA sequence allows volumetric, isotropic (0.78 × 0.78 × 0.78 mm), biexponential $T_{1\rho}$ assessment with corresponding fractions of the tissues with semisolid short T_2/T_2^*.

SPIN-LATTICE RELAXATION in the rotating frame ($T_{1\rho}$) has been proposed for different musculoskeletal applications such as detecting early-stage osteoarthritis (OA).[1] The $T_{1\rho}$ relaxation time can quantify the biochemical changes associated with proteoglycans (PG), water content, and disruption of collagen and anisotropy.[1]

In addition to hyaline articular cartilage, OA affects several other tissues such as the deep meniscus, tendon, ligament, radial and calcified layers of cartilage, and subchondral bone. Hence, $T_{1\rho}$ and T_2 relaxation study of these tissues may provide a better evaluation of OA.[2,3] However, these highly organized anisotropic tissues have very short T_2 values and as a result are not visible in the images acquired by standard sequences (GRE or FSE) with echo times (TEs) in the range of few milliseconds. Ultrashort echo time (UTE)[4] and zero echo time (ZTE)-based pulse sequences[5] employ specialized acquisition and reconstruction techniques to visualize semisolid short-T_2 tissues in vivo.

In UTE pulse sequences, the data acquisition starts as soon as possible after application of the RF pulses. The readout gradient is turned on at the same time, and the data are acquired on a center-out *k*-space trajectory such as radial,[4] spirals,[6] cones,[7] or twisted projections[8] in 2D or 3D mode.

Similar to UTE techniques, in ZTE pulse sequences the data acquisition starts with minimum delay after RF excitation. However, unlike UTE, the readout gradients are turned on before application of the RF pulse,[5] and hence, the center of *k*-space is traversed at the echo time of zero. Due to a mandatory delay for switching the hardware from transmitting to receive mode, the center of *k*-space is not sampled, and data acquisition begins at some minimum *k*-space radius. Several strategies are proposed in the literature to fill in the center of *k*-space such as algebraic reconstruction,[9] single-point imaging (SPI),[10] and water- and fat-suppressed proton projection (WASPI).[11]

The comparison of ZTE and UTE sequences in qualitative knee imaging has been discussed in previous studies.[12,13] Lee et al[12] showed that both UTE and ZTE pointwise encoding time reduction with radial acquisition (PETRA)[10] sequences could visualize the short T_2 tissues and the signal intensity in the images from both sequences was significantly lower in the patients with a meniscal tear in comparison with the normal group. The PETRA images also showed significant differences between the normal group and patients with degenerated menisci. In another study, Larson et al[13] reported similar contrast and signal-to-noise ratio (SNR) efficiency between ZTE and UTE pulse sequences for volumetric imaging of ultrashort T_2 components at 7 T. The UTE images suffer from fidelity artifacts, while shading artifact was observed in ZTE images. However, methods of correction for both of these artifacts exist.[13] Radial UTE MRI sequences can also suffer from image blurring

because of off-resonance and fast T_2^* signal decay. Kobayashi et al[14] proposed a gradient-modulated technique to reduce the blurring for the PETRA sequence.

For quantitative imaging of fast-relaxing tissues, different techniques such as the 3D-UTE,[7,15] the 2D-UTE,[16–18] and the stack of spirals (AWSOS),[19] have been proposed. Du et al proposed a UTE-$T_{1\rho}$ sequence for imaging the meniscus and Achilles tendon.[20] Other studies have investigated the suitability of quantitative T_2^* mapping in the Achilles tendon.[21,22] Moreover, Williams et al[23] proposed measuring T_2^* as a marker for subclinical changes in menisci after an anterior cruciate ligament tear.

Different water compartments in the tissues have different $T_{1\rho}$ or T_2 relaxation components. For example, in most of the knee joint structures, including patellar tendon (PT), posterior cruciate ligament (PCL), and anterior cruciate ligaments (ACL), have both dominant bound/restricted water compartment associated with collagen and/or proteoglycans, and minor less restricted / free water compartment associated with macromolecules. Several studies showed the short component sensitivity to pathology by comparing the short T_2^* component between healthy and patient groups.[24,25] In this article we propose a technique based on PETRA[10] sequence for biexponential $T_{1\rho}$ relaxation mapping in the semisolid short T_2/T_2^* relaxing tissues such as tendons and ligaments.

Materials and Methods

3D-$T_{1\rho}$-PETRA Pulse Sequence

Figure 1 illustrates the pulse sequence diagram and *k*-space trajectory of the 3D $T_{1\rho}$-PETRA sequence. The PETRA sequence[10] was modified to integrate the $T1_\rho$ preparation module with the capability of varying the spin-lock pulse duration. The sequence consists of an optional chemical shift-based fat suppression module (Fig. 1.a1), self-compensated paired $T_{1\rho}$ preparation module (Fig. 1.a2), PETRA hybrid readouts (Fig. 1.a3), and a delay for longitudinal magnetization recovery for reducing T_1 contamination (Fig. 1.a4).

The $T_{1\rho}$ preparation module starts with a 90 excitation pulse along the x-axis followed by a low-power spin lock pulse along the y-axis and a −90 pulse in the x-axis to tip the magnetization back to its initial direction along the z-axis. A 180 refocusing pulse was applied along the y-axis in the middle of the module to compensate for the B_0 inhomogeneity effect. Moreover, the spin-lock pulse was divided into four segments with altering phase to compensate the B_1 inhomogeneities.[26]

The PETRA imaging sequence consists of two readouts (radial, and a Cartesian single point imaging [SPI]) acquisition part and has been described previously.[10] The high spatial frequency data are acquired using radial spokes evenly distributed over a sphere in the *k*-space (Fig. 1.a3.1) while the center of *k*-space is acquired in the Cartesian part, which results in a low-resolution image.[10] In this method, the gradients are turned on first, and after the gradient ramp up, a hard low flip angle pulse is applied followed immediately by readout after a necessary delay time for T/R switching. The gradients have constant amplitude during the excitation and readout. The center of *k*-space was not sampled in the radial part

since it is located at the center of the excitation pulse before the mandatory delay of 70 μs for hardware switching. These essential missing central *k*-space points are acquired in the Cartesian part of the sequence, one by one, with a stepwise variation of the gradient amplitude (Fig. 1.a3.2).[10] The overall acquisition scheme is segmented in the sense of adding one $T_{1\rho}$ preparation module before each segment of *n* consecutive PETRA acquisitions and one delay time after each segment. The contrast-relevant inner Cartesian part of *k*-space is reordered according to the distance to the center of *k*-space such that the amount of $T_{1\rho}$ weighting is strongest for the points closest to the center of *k*-space.

Fat suppression was achieved by adding a fat suppression pulse[10] in front of the $T_{1\rho}$ preparation module for each segment.

Quantitative measurement of $T_{1\rho}$ was achieved by acquiring 3D-$T_{1\rho}$-PETRA scans at a series of spin-lock times (T_{sl}).

The implementation of the reconstruction is based on the Grodzki et al method,[10] which provides clinical image quality. The weight of the radial sampling points is scaled inversely to the sampling density and adapted to the density of the Cartesian grid at the center of *k*-space to ensure a smooth transition between radial and Cartesian sampling.

$T_{1\rho}$ Relaxation Mapping

The monoexponential relaxation times were calculated voxel-by-voxel by fitting the signal intensity decay over time to:

$$S(T_{sl}) = f_m \exp\left(-\frac{T_{sl}}{T_{1\rho,m}}\right) + s_0 \quad (1)$$

Where f_m is the amplitude of the exponential term, $T_{1\rho,m}$ is the monoexponential relaxation time, T_{sl} is the spin-lock pulse duration, and s_0 is a constant considering the residual noise.

Subsequently, the biexponential relaxation components were calculated in the same manner by fitting the data to:

$$S(T_{sl}) = f_s \exp\left(-\frac{T_{sl}}{T_{1\rho,s}}\right) + f_l \exp\left(-\frac{T_{sl}}{T_{1\rho,l}}\right) + s_0 \quad (2)$$

Where $T_{1\rho,s}$ and $T_{1\rho,l}$ corresponds to the short and long relaxation time components, respectively. $0 \le f_s \le 1$ and $f_l = 1 - f_s$ are the fractions of the short the long components, respectively.

In the final biexponential fitting map, the pixels that did not satisfy the following conditions were excluded from the map:

$$(f_s > \alpha_s)\&(f_l > \alpha_l)\&(F_{\text{ratio}} > \alpha_F) \quad (3)$$

where α_s and α_l are the minimum short and long fractions as was set to 10%[27] and α_F = 4.32 are the threshold based on the P = 0.1 F-distribution table for p_1 = 2 and p_2 = 4 degree of freedom in the mono- and biexponential models, respectively. The F_{ratio} is calculated as:

$$F_{ratio} = \frac{\frac{SSE_m - SSE_b}{p_2 - p_1}}{\frac{SSE_b}{L - p_2}} \quad (4)$$

where SSE_m and SSE_b are the sum of square error for the mono- and biexponential models, respectively. L is the number of T_{sl} timepoints acquired for fitting.[27]

Monte Carlo Simulations

The sensitivity of the biexponential fitting procedure to SNR, number of acquired T_{sl}, as well as the fitting error for tissues with different relaxation values was explored with Monte Carlo simulations. A set of signals was generated with a different set of T_{sl}, SNR, and $T_{1\rho}$ relaxation times. A random complex noise with normal distribution N(0, σ) with $\sigma = 1/^{\text{SNR}}$ was added to the signal. The magnitude of the complex signal is then used as a signal with Rician noise. The relaxation components were then estimated by fitting the biexponential model to the noisy signal. The process was repeated for 1000 independent noise trails, and the median of normalized absolute deviation (MNAD) was calculated for each parameter as:

$$MNAD = median\left(\frac{|y_e - y_a|}{(y_e + y_a)/2}\right), \quad (5)$$

where y_a and y_e are the actual and estimated values, respectively.

Phantom Study

The 3D $T_{1\rho}$-PETRA techniques were applied to a phantom consisting of a tube of 3% agarose (simulating biological tissue or cartilage),[28] a tube of vegetable oil (simulating fat), and a piece of a rubber eraser, simulating the tissue with semisolid short T_2 relaxation times. $T_{1\rho}$-weighted scans were acquired with spin-lock frequency (F_{sl}) = 500 Hz at different T_{sl} including 0 msec, 0.5 msec, 1 msec, 2 msec, 3.5 msec, 5 msec, 10 msec, 20 msec, and 30 msec. The fat suppression and $T_{1\rho}$ preparation modules were applied at every 26 readouts to minimize the image acquisition time, resulting in a segment size of 26. The imaging parameters were repetition time / echo time (TR/TE): 5/0.07 msec, field of view (FOV): 200 × 200 mm, flip angle: 6, slice thickness: 0.78 mm, matrix size = 256 × 256 × 256, nominal voxel size: 0.78 × 0.78 × 0.78 mm, receiver bandwidth = 399 Hz/px, T_1 recovery delay = 500 msec, number of radial spokes = 8000, number of segments = 350, number of readouts in each segment = 26, and number of Cartesian sample points = 1419. The total scan time was 33:45 minutes. To avoid any slice selectivity of the pulse, a short RF excitation pulse (60 μs), was used to enable higher excitation bandwidths; however, the flip angle is limited due to maximum available B_1 and specific absorption rate (SAR) constraint.[10]

Ex Vivo Bovine Study

Fresh bovine whole knee joint and Achilles tendon specimens (n = 2) were obtained from a slaughterhouse (Max Insel Cohen, Livingston, NJ). The tissue was covered with Parafilm to avoid dehydration during the MRI scans. The tissues were at MRI room temperature before starting the scans. $T_{1\rho}$-weighted images were acquired from the specimens. The scans were performed in the sagittal plane with F_{sl} = 500 Hz at nine different T_{sl} including 0 msec, 0.5 msec, 1 msec, 2 msec, 3.5 msec, 5 msec, 10 msec, 20 msec, and 30 msec. To examine the T_1 effect on the $T_{1\rho}$ estimation, the ex vivo bovine specimen experiments were repeated with a 2-sec T_1 restoration delay. The rest of the parameters were kept the same. The total scan time was increased to 112:57 minutes. The actual T_1 value of the ex vivo bovine specimens were also measured by acquiring T_1-weighted scans with 13 different inversion recovery times (TI) including 100 msec, 200 msec, 300 msec, 400 msec, 500 msec, 600 msec, 700 msec, 800 msec, 900 msec, 1000 msec, 1200 msec, 1500 msec, and 2000 msec using the same PETRA readout.

In Vivo Study

Ten healthy volunteers without any clinical symptoms of OA or other knee injuries were recruited for knee and ankle study (five volunteers for each study) with a mean age of 30 ± 4 years, mean weight of 63 ± 15 kg, and mean height of 169 ± 12 cm. The study was approved by the Institutional Review Board (IRB), and all the volunteers provided written informed consent prior to the MRI scan. All the scans were performed on a 3 T whole-body clinical MRI scanner (Magnetom Prisma, Siemens Healthcare, Erlangen, Germany) with a 15-channel Tx/Rx knee coil (QED, Cleveland, OH) and 16-channel foot/ankle coil (Siemens Healthcare).

Fat-suppressed $T_{1\rho}$-weighted scans were acquired using the 3D-$T_{1\rho}$-PETRA sequence with F_{sl} = 500 Hz at 9 T_{sl} durations including 0 msec, 0.5 msec, 1 msec, 2 msec, 3.5 msec, 5 msec, 10 msec, 20 msec, and 30 msec. The rubber was taped to the joint as a reference. A fat

suppression module was applied to eliminate any blurring and chemical artifacts and to increase the dynamic range of tendons and ligaments signal.[29,30] The sequence acquisition parameters were identical to the phantom study with the total scan time of 33:45 minutes. The $T_{1\rho}$-weighted images were also acquired using a customized turbo fast low angle shot (TFL) sequence[31,32] for comparison. The result is presented in the Supporting Material (Fig. S1).

Data Analysis

Monoexponential and biexponential models were fitted to the signal decay over time using the trust-region algorithm. The $T_{1\rho}$ components were calculated pixel-by-pixel over five consecutive slices for each volunteer in four regions of interest (ROIs) including the knee PT, ACL, PCL, and ankle Achilles tendon (AT). The AT was divided further into five segments: intramuscular tendon (IMT), free proximal (FPT), free mid-tendon (FMT), free distal tendon (FDT), and calcaneal tendon (CT).[33]

All the scripts were written in MatLab (R2017b, MathWorks, Natick, MA). ROIs were manually drawn in ITK-Snap and exported to MatLab for relaxation analysis.

Statistical Analysis

Statistical analysis was performed using MatLab. A pairwise nonparametric Kruskal–Wallis test was performed to assess differences in $T_{1\rho}$ values measured using the monoexponential and biexponential models among the nine different ROIs in ankle and knee. The post-hoc Dunn's test with the significant level of $\alpha = 0.05$ was performed for multiple comparisons.

Results

Monte Carlo Simulations

The Monte Carlo simulation results are shown in Fig. 2. The simulation showed (Fig. 2a) less than 10% error in the measurement of all components with SNR >50. Under the given SNR, acquiring scans with a fewer number of T_{sl} is desired to shorten the total scan time. As shown in Fig. 2b, there is less than 2% error difference between 15 and 9 T_{sl}. The improvement is negligible considering the cost of more than 50% increase in the scan time; hence, 9 T_{sl} were acquired in in vivo studies. Figure 2c,d shows the fitting error for different short and long components, respectively, while Fig. 2e,f demonstrated the effect of fractions. The component with a higher fraction has less estimation error.

Phantom and Ex Vivo Bovine Study

Figure 3a shows a representative slice at different T_{sl}. The phantom signal decay over time and the rubber eraser signal disappeared at longer T_{sl} due to its very short T_2. Figure 3b shows the signal decay and the exponential fit at a representative voxel. The phantom experiments demonstrated an average $T_{1\rho}$ of 0.86±0.37 msec for the rubber eraser.

Table 1 shows the results of the ex vivo study on the bovine knee joint and AT. The relaxation maps from a representative slice are demonstrated in Fig. 4.

The comparison between the experiment with 500 msec and 2000 msec T_1 restoration delay showed a 2% difference in estimating the monoexponential relaxation. The T_1 median and interquartile range (IQR) were 623.36(57.38) ms, 570.08 (47.68) ms, and 349.16(70.14) ms in ACL, PCL, and AT, respectively. The representative T_1 and $T_{1\rho}$ relaxation maps and fits are shown in Supporting Information Figs. S2 and S3, respectively.

In Vivo Study

The $T_{1\rho}$ descriptive statistics from the in vivo study are summarized in Table 1. The SNRs (mean ± SD) were 46 ± 8.9 and 32.7 ± 5.5 in the ankle and knee study, respectively. The representative relaxation maps in different ROIs in knee and ankle joints are demonstrated in Fig. 5. Based on the F_{ratio} criterion in Eq. [3], 79 ± 37% of the voxels in AT, 85 ± 6% of the voxels in PT, 64 ± 41% of the voxels in ACL, and 76 ± 30% of the voxels in PCL were included in the biexponential maps. The histogram distribution of relaxation components in each ROI are shown in Fig. 6.

Figure S4 shows axial reformatted slices from fat-suppressed $T_{1\rho}$-weighted PETRA images of a volunteer. Slices at five different positions along the Achilles tendon including the 1) intramuscular tendon, 2) free proximal tendon, 3) free mid-tendon, 4) free distal tendon, and 5) calcaneal tendon are presented. The ability to evaluate the relaxation maps from different views is shown in Fig. 7.

The comparison of fit residuals of the mono- and biexponential models (Fig. S5) showed that the biexponential model better represented the $T_{1\rho}$ relaxation decay than the monoexponential model. The Kruskal–Wallis followed by post-hoc Dunn's tests for each component revealed significant differences between relaxation components in several ROIs. The results of pairwise comparisons is shown in Table 2.

Discussion

In this article we present a ZTE MRI technique based on a PETRA sequence for in vivo, bicomponent $T_{1\rho}$ relaxation mapping of semisolid short-T_2 tissues such as ligaments and tendons on a 3 T scanner. To the best of our knowledge, this is the first work proposing a ZTE sequence for bicomponent $T_{1\rho}$ analysis of semisolid tissues with very short T_2 values. ROIs were defined in the PT, ACL, and PCL of the knee joints and AT of the ankle joint, and mono- and biexponential $T_{1\rho}$ relaxation components were measured in each ROI. The results showed that biexponential fitting might better distinguish the short relaxation time associated with the restricted water in the macromolecules. The isotropic spatial resolution allowed the multiplanar reformatting of the scans and evaluation of the relaxation, in any plane, and hence the complete coverage of the surface of the tendons and ligaments.

The higher bandwidth required for 3D excitation was achieved using a very short hard RF excitation pulse. This allows for limited flip angles due to available maximum B_1 amplitude and limited pulse duration. Li et al[34] proposed a variable flip angle method using a quadratic phase-modulated RF excitation pulse to achieve maximal transverse magnetization and equal amplitude of the short-T_2 signal. However, the method cannot be used for relaxation

mapping since the signal amplitude becomes dependent on the flip angles in addition to the $T_{1\rho}$ decay.

The 8000 radial spokes acquired in this experiment covers about 4% of full Nyquist sampling ($256 \times 256 \times \pi = 205{,}887$), which results in image blurring. As shown in Supporting Information Fig. S6, increasing the number of spokes from 8000 to 24,000 will reduce the blurring at the cost of increasing the scan time.

The bandwidth of the fat sat (FS) pulse was 220 Hz (half of the chemical shift w.r.t. water) and its duration was 5120 μs. The fat suppression was less effective in longer TSLs. However, it is not possible to put the fat suppression module after $T_{1\rho}$ preparation, due the long duration of the FS pulse.

The results of the ex vivo study are in agreement with the in vivo measurement. Our $T_{1\rho,m}$ of 6.50 ± 3.37 msec in AT is in agreement with the Du et al[20] study (4.95 ± 0.23 msec). The reported values for $T_{1\rho,m}$ for ACL and PCL in the Ma et al[35] study (ACL: 34.9 ± 2.8 msec, PCL: 21.6 ± 1.4 msec) are higher than $T_{1\rho,m}$ of 21.8 ± 6.3 msec and 16.2 ± 4.1 msec in our study for ACL and PCL, respectively. The reason could be due to the $T_{1\rho}$ dispersion effect as a result of using adiabatic spin-locking pulses in the Ma et al study.

The bicomponent $T_{1\rho}$ analysis of bound and free water in various knee joint tissues and the muscle was reported previously[31,32,36] employing conventional readouts (TFL). Juras et al[25] reported the bicomponent T_2^* analysis of AT using a variable-echo-time (vTE) technique and showed the significant difference for short component between healthy and diseased AT. The longer TEs >800 μs used in that study in comparison with our study (TE = 70 μs) makes the technique more sensitive to the long component than the short component.

The proposed sequence supported using chemical shift-based fat suppression pulses for contrast generation. However, our results showed it is less effective at longer T_{sl}. One possible reason could be the segmented structure of the sequence. The fat suppression pulse was applied once prior to the $T_{1\rho}$ preparation module followed by a set of excitation pulses. It cannot be applied before each excitation due to the time constraints. The short T_1 of the fat leads to its partial signal recovery between two consecutive FS pulses.

The application of a long continuous wave spin-lock pulse makes the sequence SAR-intensive. In our proposed technique, the 500 msec delay used for T_1 recovery also eliminates the SAR constraint. Real-time SAR monitoring during the in vivo scans confirmed that it was always below the US Food and Drug Administration (FDA) limit (<50%).

We have only demonstrated the technical feasibility of the 3D $T1_\rho$-PETRA sequence in providing volumetric bicomponent analysis of semisolid tissues with very short T_2 in a rubber eraser phantom, ex vivo bovine knee joint, and in vivo knee joint applications. No patients were recruited for this study and the study group was fairly small. Further repeatability and reproducibility experiments are also warranted to validate the proposed technique. Second, the magic angle effect can influence the $T_{1\rho}$ value due to the dipolar interactions of fiber orientation with respect to B_0. While the PT and AT are parallel to B_0

and the PCL is orthogonal to B_0, the orientation degree of the tibial part of the ACL to B_0 is close to the magic angle.[37] Application of the higher spin-lock frequency (1–2 KHz) to diminish the magic angle effect is not feasible for in vivo studies due to the SAR constraints. Moreover, as shown by Wang and Xia,[38] only the single relaxation behavior is observed at a higher spin-lock field. Hence, a 500 Hz spin-lock frequency was selected in this study as a good trade-off between reducing the magic angle effect and observing the biexponential behavior.

There is large uncertainty of the fitted parameters due to the nature of the biexponential model for relaxation decay, and in the presence of noise several equally well-fitted combinations of parameters can be found.[39] Several investigators proposed methods to improve the fitting of multicomponent signals, including using a priori information to stabilize the fitting process and optimizing the acquisition parameters.[40] Recently, Anastasiou and Hall[41] used Cramer–Rao theory and simulations to show that the T_2 fit errors were minimized by maximizing the SNR of the images acquired, as well the number of points used in the fitting procedure and by using a biexponential system with a high T_{22}/T_{21} ratio. However, acquiring more timepoints and increasing the SNR requires a longer scan time. In our study, the total scan time of ~34 minutes needed to acquire 9 T_{sl} is too long for clinical use. We will plan on using compressed sensing and deep learning reconstruction techniques to further reduce the acquisition time in our future study. The technique can be potentially applied to other applications such as studies of calcified cartilage layer, cortical bone, and myelin in addition to studying ligaments and tendon disorders.

In conclusion, the 3D $T_{1\rho}$-PETRA technique provides a robust volumetric bicomponent $T_{1\rho}$ mapping of semisolid short T_2 tissues such as ACL, PCL, and PT in the knee joint and AT in the ankle joint.

Supplementary Material

Refer to Web version on PubMed Central for supplementary material.

Acknowledgment

Contract grant sponsor: National Institutes of Health (NIH); Contract grant numbers: R01 AR067156, and R01 AR068966, performed under the rubric of the Center of Advanced Imaging Innovation and Research (CAI2R), an NIBIB Biomedical Technology Resource Center (NIH P41 EB017183).

The authors thank Matthias Fenchel, PhD, Siemens Healthineers, for technical assistance.

References

1. Regatte RR, Akella SV, Lonner J, Kneeland J, Reddy R. T1ρ relaxation mapping in human osteoarthritis (OA) cartilage: Comparison of T1ρ with T2. J Magn Reson Imaging 2006;23:547–553. [PubMed: 16523468]
2. Brandt KD, Radin EL, Dieppe PA, van de Putte L. Yet more evidence that osteoarthritis is not a cartilage disease. Ann Rheum Dis 2006;65: 1261–1264. [PubMed: 16973787]
3. Tan AL, Toumi H, Benjamin M, et al. Combined high-resolution magnetic resonance imaging and histological examination to explore the role of ligaments and tendons in the phenotypic expression of early hand osteoarthritis. Ann Rheum Dis 2006;65:1267–1272. [PubMed: 16627540]

4. Gatehouse PD, Bydder GM. Magnetic resonance imaging of short T2 components in tissue. Clin Radiol 2003;58:1–19. [PubMed: 12565203]
5. Hafner S Fast imaging in liquids and solids with the Back-projection Low Angle ShoT (BLAST) technique. Magn Reson Imaging 1994;12: 1047–1051. [PubMed: 7997092]
6. Du J, Bydder M, Takahashi AM, Chung CB. Two-dimensional ultrashort echo time imaging using a spiral trajectory. Magn Reson Imaging 2008; 26:304–312. [PubMed: 18096346]
7. Chen B, Zhao Y, Cheng X, et al. Three-dimensional ultrashort echo time cones (3D UTE-Cones) magnetic resonance imaging of entheses and tendons. Magn Reson Imaging 2018;49:4–9. [PubMed: 29309823]
8. Boada FE, Gillen JS, Shen GX, Chang SY, Thulborn KR. Fast three dimensional sodium imaging. Magn Reson Med 1997;37:706–715. [PubMed: 9126944]
9. Weiger M, Hennel F, Pruessmann KP. Sweep MRI with algebraic reconstruction. Magn Reson Med 2010;64:1685–1695. [PubMed: 20949600]
10. Grodzki DM, Jakob PM, Heismann B. Ultrashort echo time imaging using pointwise encoding time reduction with radial acquisition (PETRA). Magn Reson Med 2012;67:510–518. [PubMed: 21721039]
11. Wu Y, Hrovat MI, Ackerman JL, et al. Bone matrix imaged in vivo by water- and fat-suppressed proton projection MRI (WASPI) of animal and human subjects. J Magn Reson Imaging 2010;31:954–963. [PubMed: 20373441]
12. Lee YH, Suh J-S, Grodzki D. Ultrashort echo (UTE) versus pointwise encoding time reduction with radial acquisition (PETRA) sequences at 3 Tesla for knee meniscus: A comparative study. Magn Reson Imaging 2016;34:75–80. [PubMed: 26435460]
13. Larson PEZ, Han M, Krug R, et al. Ultrashort echo time and zero echo time MRI at 7T. Magn Reson Mater Phys Biol Med 2016;29:359–370.
14. Kobayashi N, Goerke U, Wang L, Ellermann J, Metzger GJ, Garwood M. Gradient-Modulated PETRA MRI. Tomography 2015;1:85. [PubMed: 26771005]
15. Ma YJ, Carl M, Shao H, Tadros AS, Chang EY, Du J. Three-dimensional ultrashort echo time cones T1ρ (3D UTE-cones-T1ρ) imaging. NMR Biomed 2017;30:e3709.
16. Du J, Carl M, Bae WC, et al. Dual inversion recovery ultrashort echo time(DIR-UTE) imaging and quantification of the zone of calcified cartilage (ZCC). Osteoarthritis Cartilage 2013;21:77–85. [PubMed: 23025927]
17. Du J, Carl M, Bydder M, Takahashi A, Chung CB, Bydder GM. Qualitative and quantitative ultrashort echo time (UTE) imaging of cortical bone. J Magn Reson 2010;207:304–311. [PubMed: 20980179]
18. Du J, Diaz E, Carl M, Bae W, Chung CB, Bydder GM. Ultrashort echo time imaging with bi-component analysis. Magn Reson Med 2012;67:645–649. [PubMed: 22034242]
19. Qian Y, Boada FE. Acquisition-weighted stack of spirals for fast high-resolution three-dimensional ultra-short echo time MR imaging. Magn Reson Med 2008;60:135–145. [PubMed: 18581326]
20. Du J, Carl M, Diaz E, et al. Ultrashort TE T1rho (UTE T1rho) imaging of the Achilles tendon and meniscus. Magn Reson Med 2010;64:834–842. [PubMed: 20535810]
21. Juras V, Zbyn S, Pressl C, et al. Regional variations of T2* in healthy and pathologic Achilles tendon in vivo at 7 Tesla: Preliminary results. Magn Reson Med 2012;68:1607–1613. [PubMed: 22851221]
22. Robson MD, Benjamin M, Gishen P, Bydder GM. Magnetic resonance imaging of the Achilles tendon using ultrashort TE (UTE) pulse sequences. Clin Radiol 2004;59:727–735. [PubMed: 15262548]
23. Williams A, Qian Y, Golla S, Chu CR. UTE-T2* mapping detects subclinical meniscus injury after anterior cruciate ligament tear. Osteoarthritis Cartilage 2012;20:486–494. [PubMed: 22306000]
24. Kijowski R, Wilson JJ, Liu F. Bicomponent ultrashort echo time T2* analysis for assessment of patients with patellar tendinopathy. J Magn Reson Imaging 2017;46:1441–1447. [PubMed: 28263448]
25. Juras V, Apprich S, Szomolanyi P, Bieri O, Deligianni X, Trattnig S. Biexponential T2* analysis of healthy and diseased Achilles tendons: An in vivo preliminary magnetic resonance study and correlation with clinical score. Eur Radiol 2013;23:2814–2822. [PubMed: 23760303]

26. Mitrea BG, Krafft AJ, Song R, Loeffler RB, Hillenbrand CM. Paired self-compensated spin-lock preparation for improved T1rho quantification. J Magn Reson 2016;268:49–57. [PubMed: 27161095]
27. Zibetti MVW, Sharafi A, Otazo R, Regatte RR. Compressed sensing acceleration of biexponential 3D-T1ρ relaxation mapping of knee cartilage. Magn Reson Med 2019;81:863–880. [PubMed: 30230588]
28. Buck FM, Bae WC, Diaz E, et al. Comparison of T1rho measurements in agarose phantoms and human patellar cartilage using 2D multislice spiral and 3D magnetization prepared partitioned k-space spoiled gradient-echo snapshot techniques at 3 T. AJR Am J Roentgenol 2011;196:W174–179. [PubMed: 21257859]
29. Bydder GM, Chung CB. Magnetic resonance imaging of short T2 relaxation components in the musculoskeletal system. Skeletal Radiol 2009;38: 201–205. [PubMed: 18941741]
30. Han M, Larson PEZ, Liu J, Krug R. Depiction of Achilles tendon microstructure in vivo using high-resolution 3D ultrashort echo-time MRI at 7T. Invest Radiol 2014;49:339–345. [PubMed: 24500089]
31. Baboli R, Sharafi A, Chang G, Regatte RR. Isotropic morphometry and multicomponent T1ρ mapping of human knee articular cartilage in vivo at 3T. J Magn Reson Imaging 2018;48:1707–1716. [PubMed: 29717787]
32. Sharafi A, Xia D, Chang G, Regatte RR. Bi-exponential T1rho relaxation mapping of human knee cartilage in vivo at 3 T. NMR Biomed 2017;30(10).
33. Del Buono A, Chan O, Maffulli N. Achilles tendon: Functional anatomy and novel emerging models of imaging classification. Int Orthop 2013; 37:715–721. [PubMed: 23254856]
34. Li C, Magland JF, Zhao X, Seifert AC, Wehrli FW. Selective in vivo bone imaging with long-T2 suppressed PETRA MRI. Magn Reson Med 2017;77: 989–997. [PubMed: 26914767]
35. Ma YJ, Carl M, Searleman A, Lu X, Chang EY, Du J. 3D adiabatic T1ρ prepared ultrashort echo time cones sequence for whole knee imaging. Magn Reson Med 2018;80:1429–1439. [PubMed: 29493004]
36. Sharafi A, Chang G, Regatte RR. Bi-component T1ρ and T2 relaxation mapping of skeletal muscle In vivo. Sci Rep 2017;7:14115. [PubMed: 29074883]
37. Hayes CW, Parellada JA. The magic angle effect in musculoskeletal MR imaging. Top Magn Reson Imaging 1996;8:51–56. [PubMed: 8820094]
38. Wang N, Xia Y. Dependencies of multi-component T2 and T1ρ relaxation on the anisotropy of collagen fibrils in bovine nasal cartilage. J Magn Reson 2011;212:124–132. [PubMed: 21788148]
39. Bretthorst GL. How accurately can parameters from exponential models be estimated? A Bayesian view. Concepts Magn Reson A 2005;27A:73–83.
40. Kumar D, Nguyen Thanh D, Gauthier Susan A, Raj A. Bayesian algorithm using spatial priors for multiexponential T2 relaxometry from multiecho spin echo MRI. Magn Reson Med 2012;68:1536–1543. [PubMed: 22266707]
41. Anastasiou A, Hall LD. Optimisation of T2 and M0 measurements of biexponential systems. Magn Reson Imaging 2004;22:67–80. [PubMed: 14972396]

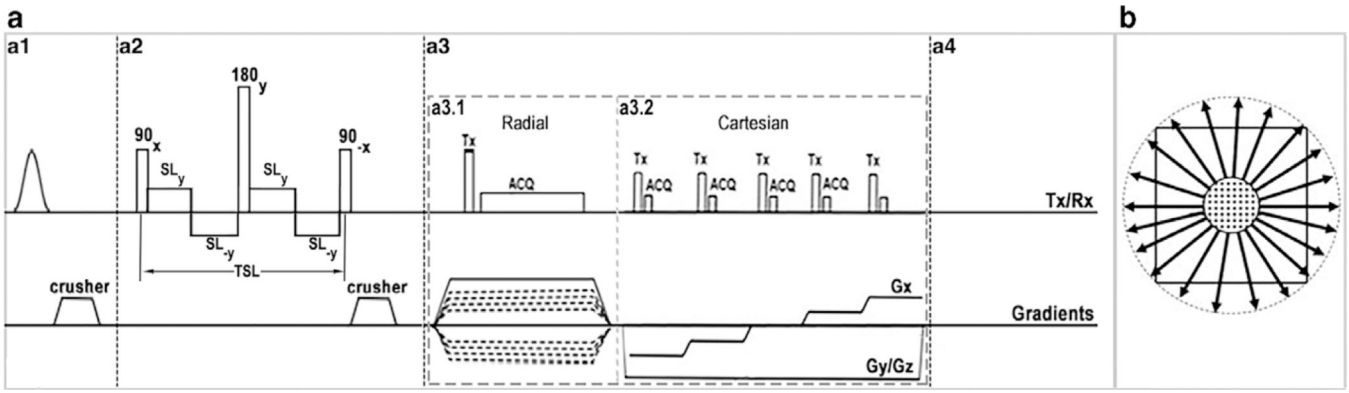

FIGURE 1:

3D-$T_{1\rho}$-PETRA (a) pulse sequence diagram and (b) *k*-space trajectory. (a1) Fat suppression module. (a2) self-compensated paired $T_{1\rho}$ preparation module. (a3) PETRA acquisition: (a3.1) radial and (a3.2) Cartesian SPI parts. (a4) Longitudinal magnetization restoration delay. (b) *k*-space trajectory. The *k*-space center is filled with Cartesian SPI while the rest is filled using the radial acquisition.

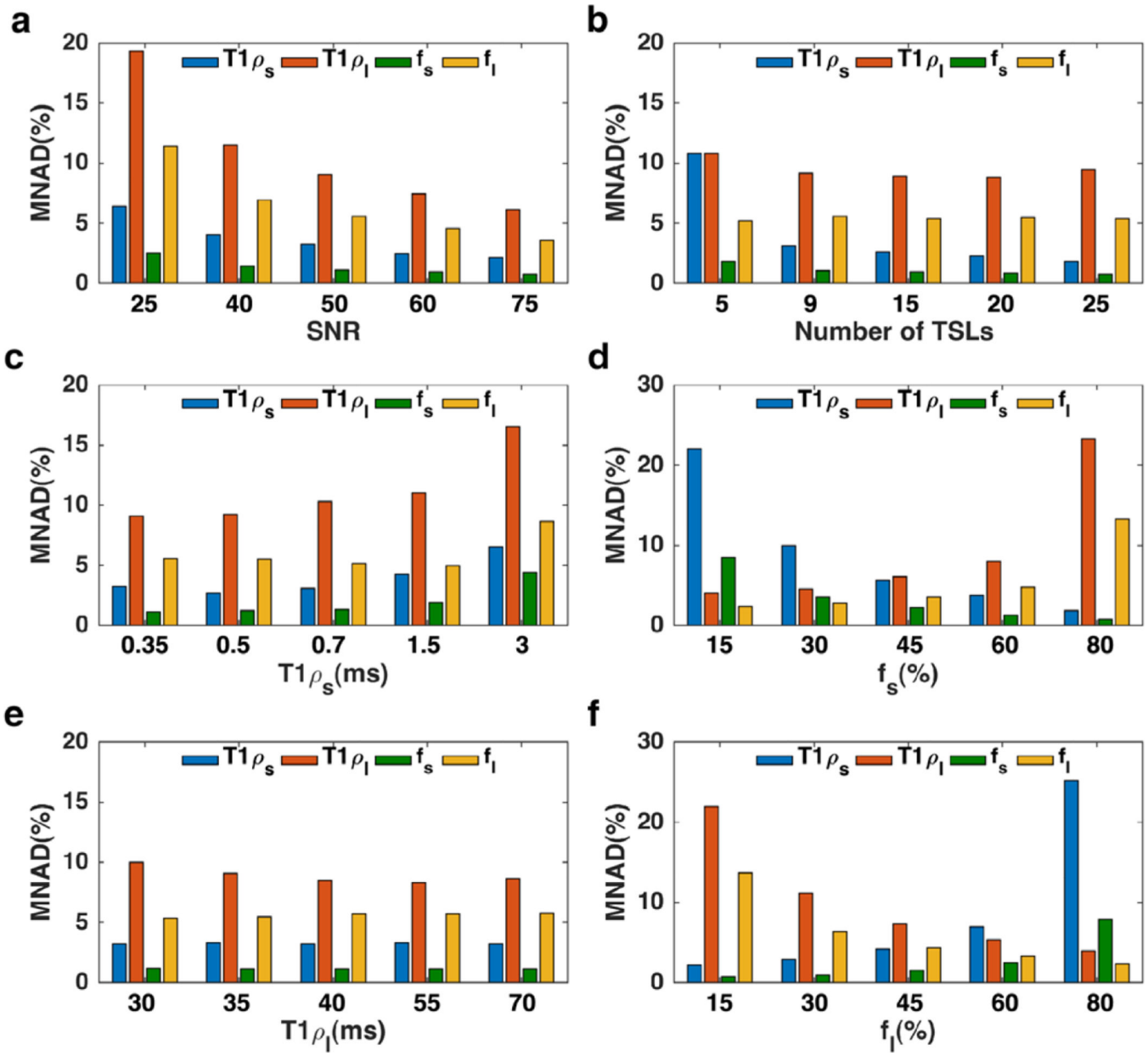

FIGURE 2:

Monte Carlo simulations. (a) The effect of SNR on biexponential estimation (b) Acquiring scan at more T_{sl} timepoints reduces the estimation error. (c) The smaller short component ($T_{1\rho}$,s) has less estimation error, (d) higher short fraction leads to a smaller error in estimating short component. (e) The shorter long component has more estimation error. (f) Higher long fraction leads to a smaller error in estimating long component.

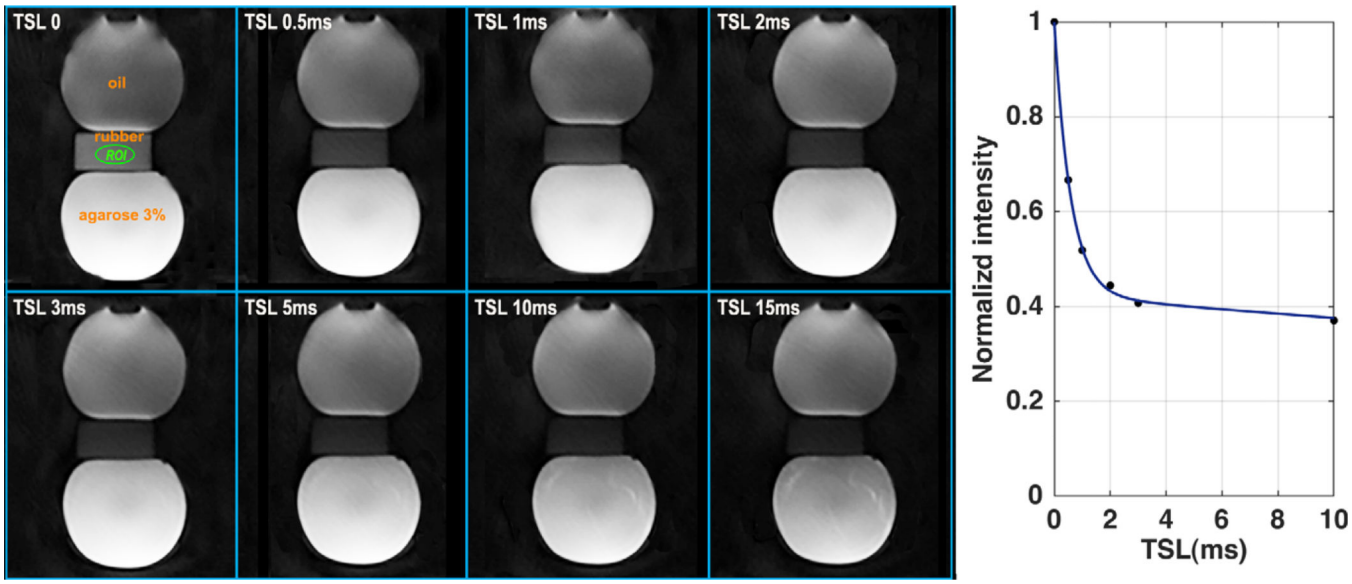

FIGURE 3:

The phantom consists of a tube of 3% agarose (simulating biological tissue or cartilage), a tube of vegetable oil (simulating fat) and a piece of a rubber eraser, simulating the tissue with semisolid short T_2 relaxation times. The oil signal is reduced due to the application of FatSat pulse. The fast $T_{1\rho}$ relaxation decay can be observed in the rubber eraser.

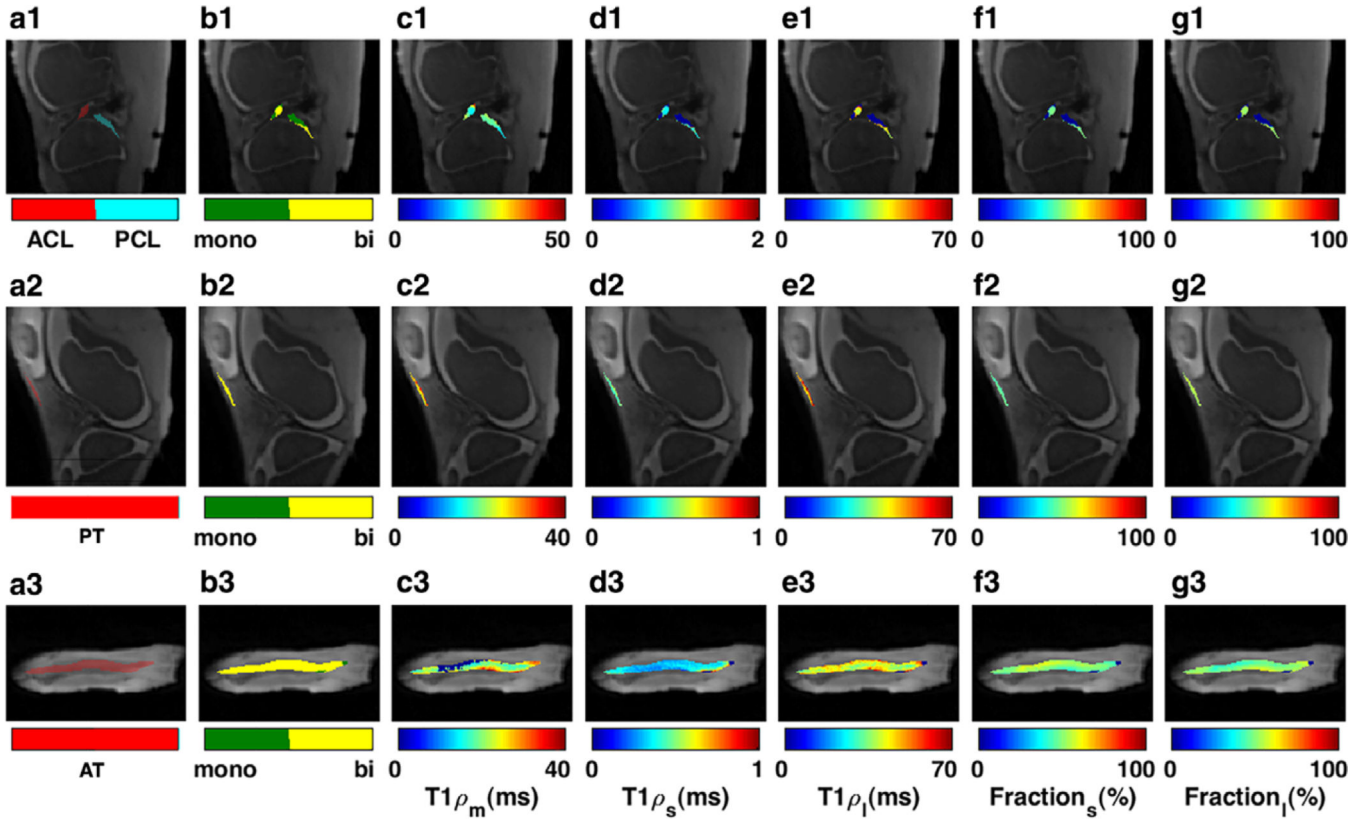

FIGURE 4:

Representative $T_{1\rho}$ maps from ex vivo bovine scans in four ROIs including (a1) Anterior and posterior cruciate ligaments, (a2) patellar tendon, and (a3) Achilles tendon. (b1–3) The binary map is showing the location of pixels included in the biexponential estimation. (c1–3) mono relaxation time, (d1–3) short $T_{1\rho}$ relaxation time, (e1–3) long $T_{1\rho}$ relaxation time, (f1–3) short $T_{1\rho}$ fraction, and (g1–3) long $T_{1\rho}$ fraction maps.

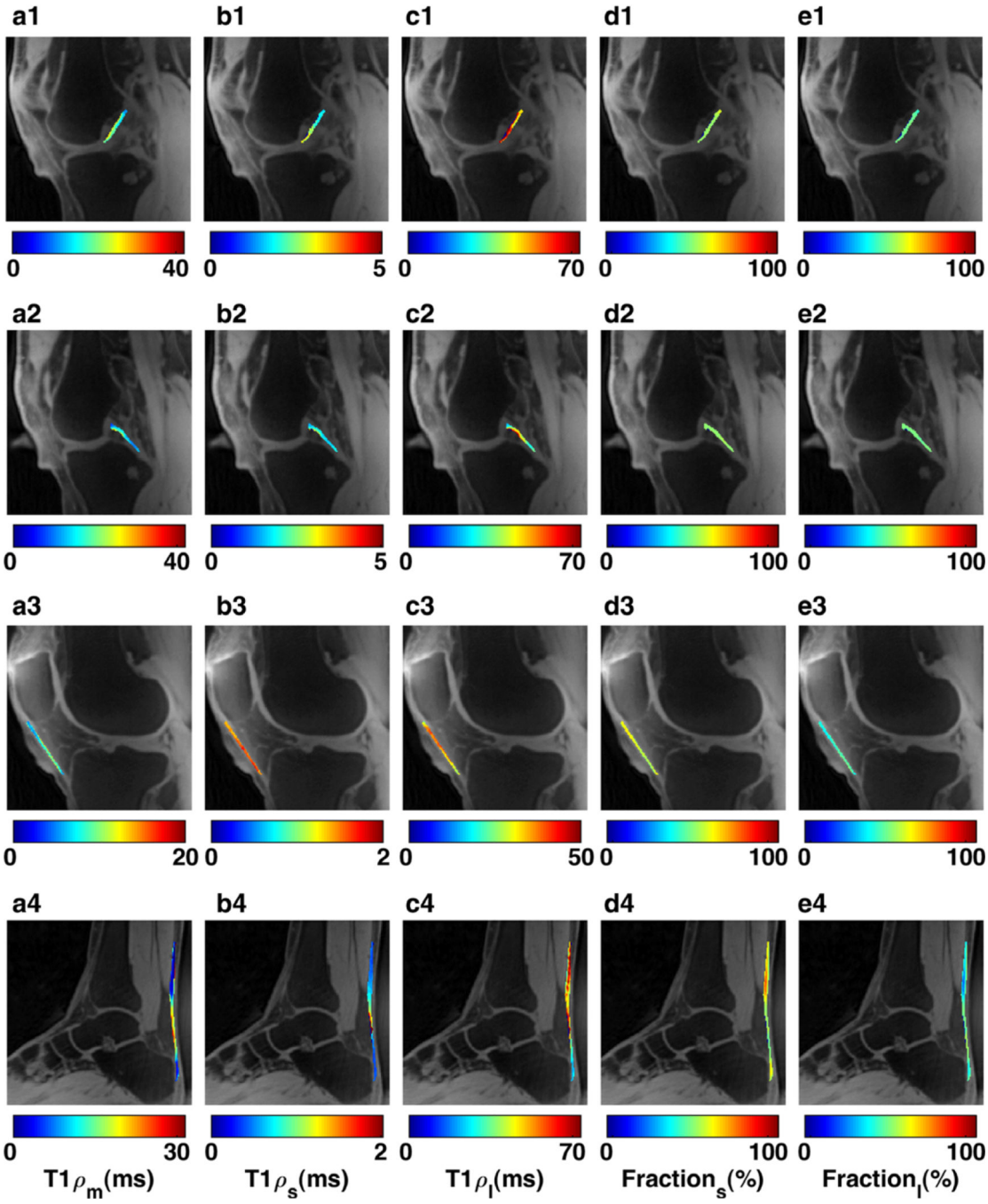

FIGURE 5:

Representative $T_{1\rho}$ maps of in vivo knee and ankle study. (a1–4) mono $T_{1\rho}$ relaxation time, (b1–4) short $T_{1\rho}$ relaxation time, (c1–4) long $T_{1\rho}$ relaxation time, (d1–4) short $T_{1\rho}$ fraction, and (e1–3) long $T_{1\rho}$ fraction maps.

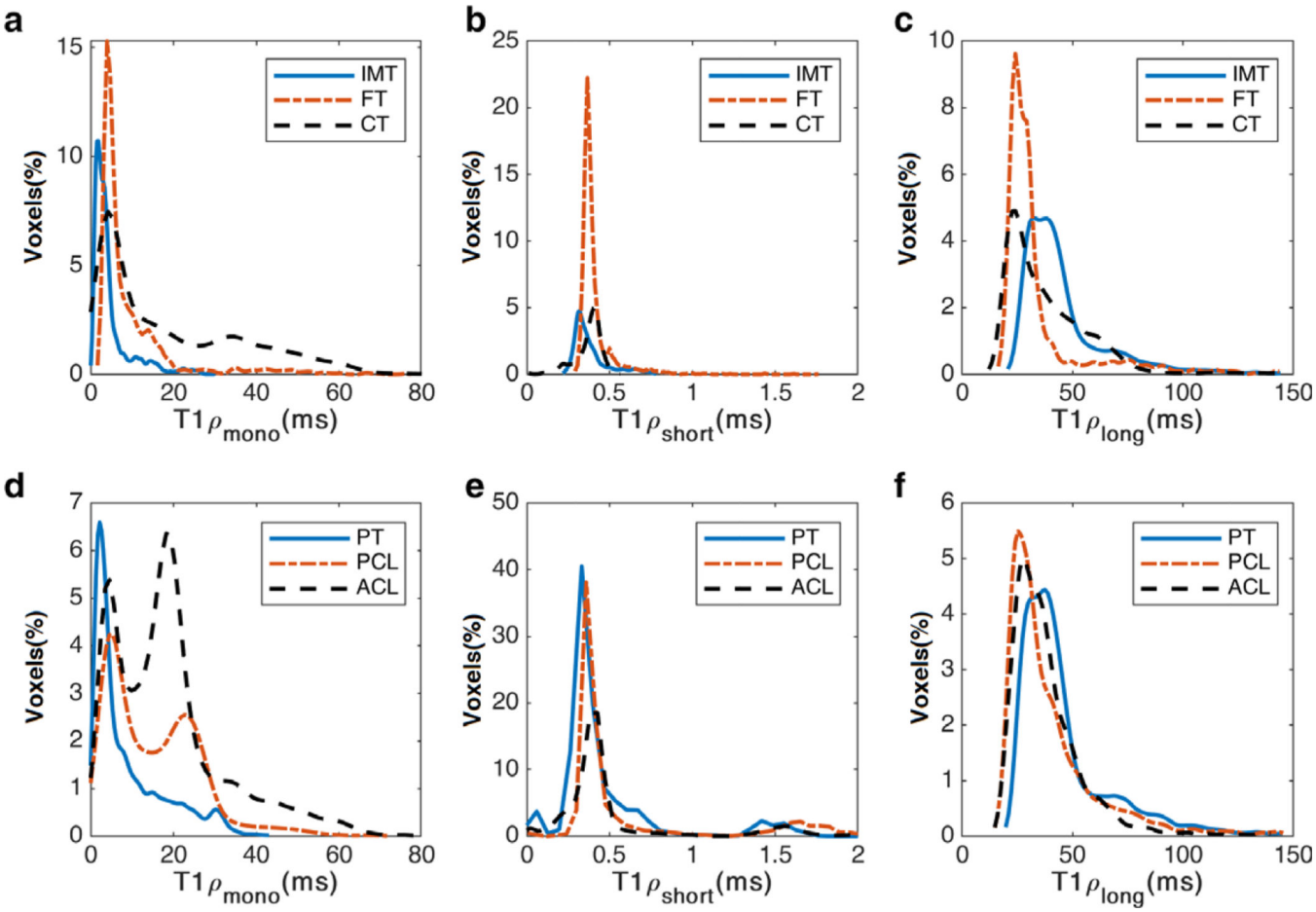

FIGURE 6:

The histogram distribution over different ROIs (a–c) ankle and (d–f) knee study for (a,d) mono (b,e) short and (c,f) long component. The y-axis shows the relative frequency for 100 bins.

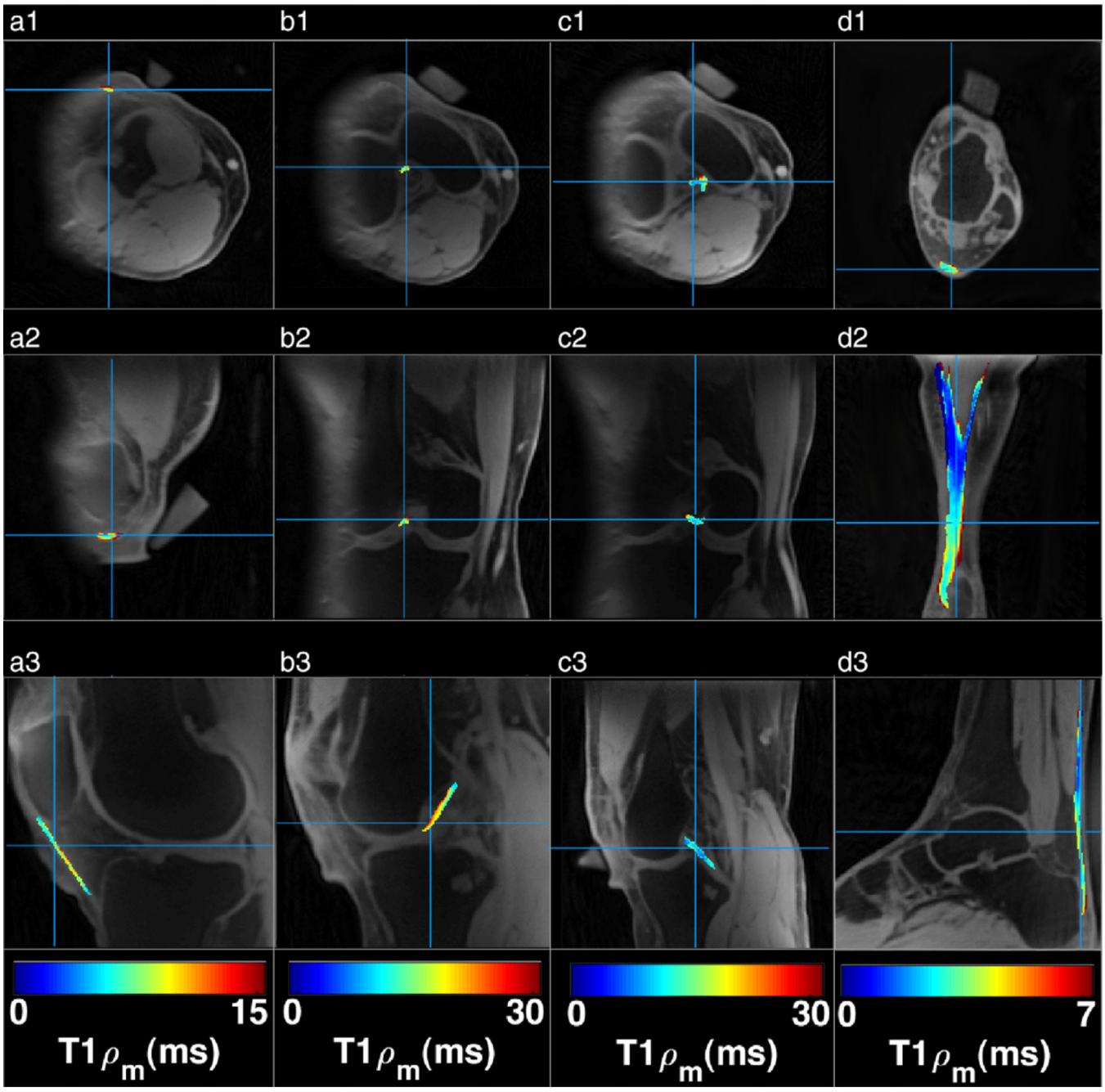

FIGURE 7:
Reformatted (a1–d1) axial and (a2–d2) coronal monoexponential maps from sagittal (a3–d3) plane in (a1–a3) patellar tendon (b1–b3) ACL, (c1–c3) PCL, and (d1–d3) Achilles tendon. The positions of reformatted slices are denoted on the corresponding maps.

TABLE 1.

Summary of ex vivo Bovine and in vivo Knee and Ankle Study

ROIs	$T_{1\rho m}$ (msec) median (IQR)	$T_{1\rho s}$ (msec) median (IQR)	$T_{1\rho l}$ (msec) median (IQR)	$Fraction_s$ (%) median (IQR))	$Fraction_l$ (%) median (IQR)
Bovine PT	26.62 (6.15)	0.42 (0.04)	41.85 (6.95)	38.04 (9.07)	61.96 (9.07)
Bovine ACL	18.16 (2.38)	0.75 (0.23)	25.87 (1.84)	26.37 (5.66)	73.63 (5.66)
Bovine PCL	12.91 (2.53)	0.64 (0.13)	27.29 (2.96)	43.89 (7.37)	57.11 (7.37)
Bovine AT	5.42 (1.68)	0.43 (0.07)	22.55 (4.99)	55.63 (5.57)	44.37 (5.57)
Knee PT	15.92 (14.49)	0.65 (1.01)	37.32 (18.36)	46.87 (15.35)	53.13 (15.35)
Knee ACL	23.61 (9.44)	1.66 (2.12)	43.69 (17.83)	42.47 (12.51)	57.53 (12.51)
Knee PCL	17.42 (7.37)	1.16 (1.86)	27.66 (14.68)	42.64 (14.03)	57.36 (14.03)
Achilles IMT	2.88 (2.20)	0.36 (0.07)	42.79 (12.67)	68.24 (7.43)	31.76 (7.43)
Achilles FPT	3.06 (1.64)	0.40 (0.33)	37.83 (9.01)	68.92 (6.69)	31.08 (6.69)
Achilles FMT	3.80 (6.07)	0.37 (0.38)	36.07 (7.64)	64.61 (5.44)	35.39 (5.44)
Achilles FDT	6.89 (6.46)	0.37 (0.04)	30.28 (9.03)	58.81 (2.67)	41.19 (2.67)
Achilles CT	3.91 (5.35)	0.38 (0.28)	35.14 (6.75)	64.05 (5.50)	35.95 (5.50)
Achilles tendon	5.78 (10.25)	0.39 (0.02)	31.34 (10.82)	58.82 (13.32)	41.18 (13.32)

Medians and interquartile range (IQR) of multicomponent $T_{1\rho}$ relaxation times and corresponding fractions in ligaments and tendons (PT, ACL, PCL, and AT).

PT: Patellar Tendon; ACL: Anterior Cruciate Ligament; PCL: Posterior Cruciate Ligament; AT: Achilles Tendon; IMT: Intramuscular Tendon FPT: Free Proximal Tendon; FMT: Free Mid Tendon; FDT: Free Distal Tendon; CT: Calcaneal Tendon

TABLE 2.

Dunn's Post-Hoc Pairwise Comparison Between Different ROIs for Mono- and Biexponential Components

ROI1	ROI2	$T_{1\rho m}$	$T_{1\rho s}$	$Fraction_s$	$T_{1\rho l}$	$Fraction_l$
ACL	**CT**	0.97	1.00	0.70	0.99	1.000
ACL	FDT	0.61	0.92	0.31	1.00	0.97
ACL*	FMT	**0.040**	0.68	**0.019**	1.00	0.37
ACL*	FPT	**0.006**	0.79	**0.003**	1.00	0.100
ACL*	IMT	**0.004**	0.44	**0.002**	1.00	0.072
ACL	PCL	1.00	1.00	1.00	1.00	1.00
ACL	PT	1.00	1.00	1.00	1.00	1.00
CT	FDT	1.00	1.00	1.00	1.00	1.00
CT	FMT	0.98	1.00	0.99	1.00	0.99
CT	FPT	0.69	1.00	0.91	0.99	0.91
CT	IMT	0.62	1.00	0.85	0.89	0.85
CT	PCL	1.00	0.74	0.95	0.99	0.95
CT	PT	1.00	1.00	0.99	1.00	0.99
FDT	FMT	1.00	1.00	1.00	1.00	1.00
FDT	FPT	0.98	1.00	0.99	1.00	0.99
FDT	IMT	0.97	1.00	0.99	0.96	0.99
FDT	PCL	0.98	0.26	0.67	1.00	0.68
FDT	PT	0.98	0.91	0.89	1.00	0.89
FMT	FPT	1.00	1.00	1.00	1.00	1.00
FMT	IMT	1.00	1.00	1.00	1.00	1.00
FMT	PCL	0.35	0.10	0.09	1.00	0.09
FMT	PT	0.33	0.66	0.20	1.00	0.21
FPT	IMT	1.00	1.00	1.00	1.00	1.00
FPT*	PCL	0.07	0.15	**0.014**	1.00	**0.014**
FPT*	PT	0.06	0.78	**0.036**	1.00	**0.036**
IMT*	PCL	**0.043**	**0.036**	**0.010**	1.00	**0.010**

ROI1	ROI2	$T_{1\rho m}$	$T_{1\rho s}$	$Fraction_s$	$T_{1\rho l}$	$Fraction_l$
IMT*	PT	**0.040**	0.42	**0.026**	1.00	**0.026**
PCL	PT	1.00	1.00	1.00	1.00	1.00

The regions with a statistically significant difference ($P < 0.05$) are shown in bold and with asterisk.

PT: Patellar Tendon; ACL: Anterior Cruciate Ligament; PCL: Posterior Cruciate Ligament; AT: Achilles Tendon; IMT: Intramuscular Tendon FPT: Free Proximal Tendon; FMT: Free Mid Tendon; FDT: Free Distal Tendon; CT: Calcaneal Tendon.